Additional shear resistance from fault roughness and stress levels on geometrically complex faults

Zijun Fang[1] and Eric M. Dunham[2,3]

[1]   The majority of crustal faults host earthquakes when the ratio of average background shear stress τ^b to effective normal stress σ^{eff} is $\tau^b/\sigma^{\text{eff}} \approx 0.6$. In contrast, mature plate-boundary faults like the San Andreas Fault (SAF) operate at $\tau^b/\sigma^{\text{eff}} \approx 0.2$. Dynamic weakening, the dramatic reduction in frictional resistance at coseismic slip velocities that is commonly observed in laboratory experiments, provides a leading explanation for low stress levels on mature faults. Strongly velocity-weakening friction laws permit rupture propagation on flat faults above a critical stress level $\tau^{\text{pulse}}/\sigma^{\text{eff}} \approx 0.25$. Provided that dynamic weakening is not restricted to mature faults, the higher stress levels on most faults are puzzling. In this work, we present a self-consistent explanation for the relatively high stress levels on immature faults that is compatible with low coseismic frictional resistance, from dynamic weakening, for all faults. We appeal to differences in structural complexity with the premise that geometric irregularities introduce resistance to slip in addition to frictional resistance. This general idea is quantified for the special case of self-similar fractal roughness of the fault surface. Natural faults have roughness characterized by amplitude-to-wavelength ratios α between 10^{-3} and 10^{-2}. Through a second-order boundary perturbation analysis of quasi-static frictionless sliding across a band-limited self-similar interface in an ideally elastic solid, we demonstrate that roughness induces an additional shear resistance to slip, or roughness drag, given by $\tau^{\text{drag}} = 8\pi^3\alpha^2 G^*\Delta/\lambda_{\text{min}}$, for $G^* = G/(1-\nu)$ with shear modulus G and Poisson's ratio ν, slip Δ, and minimum roughness wavelength λ_{min}. The influence of roughness drag on fault mechanics is verified through an extensive set of dynamic rupture simulations of earthquakes on strongly rate-weakening fractal faults with elastic-plastic off-fault response. The simulations suggest that fault rupture, in the form of self-healing slip pulses, becomes probable above a background stress level $\tau^b \approx \tau^{\text{pulse}} + \tau^{\text{drag}}$. For the smoothest faults ($\alpha \sim 10^{-3}$), τ^{drag} is negligible compared to frictional resistance, so that $\tau^b \approx \tau^{\text{pulse}} \approx 0.25\sigma^{\text{eff}}$. However, on rougher faults ($\alpha \sim 10^{-2}$), roughness drag can exceed frictional resistance. We expect that τ^{drag} ultimately departs from the predicted scaling when roughness-induced stress perturbations activate pervasive off-fault inelastic deformation, such that background stress saturates at a limit ($\tau^b \approx 0.6\sigma^{\text{eff}}$) determined by the finite strength of the off-fault material. We speculate that this strength, and not the much smaller dynamically weakened frictional strength, determines the stress levels at which the majority of faults operate.

[1]ConocoPhillips Company, Houston, Texas, USA.
[2]Department of Geophysics, Stanford University, Stanford, California, USA.
[3]Institute for Computational and Mathematical Engineering, Stanford University, Stanford, California, USA.

Corresponding author: Z. Fang, ConocoPhillips Company, 2012 Permian, 600 North Dairy Ashford Rd., Houston, TX 77079, USA. (zijun.fang@conocophillips.com)

1. Introduction

[2]   Deviatoric stresses within Earth's brittle crust are limited by the strength of faults and are generally thought to reflect the stress levels at which faults become capable of hosting earthquakes [*Townend and Zoback*, 2000]. These average stress levels are potentially distinct from, and much smaller than, localized stress concentrations at earthquake nucleation sites where the ratio of shear to effective normal stress reaches the level of static friction. Our aim in this work is to quantify the relationship between overall stresses on faults, averaged over the full extent of the largest

ruptures, and details of the dynamic rupture process on geometrically complex faults. Through numerical simulations and analytical results, we demonstrate that stress levels are determined not only by frictional resistance but also by an additional geometric resistance, from irregularities at scales larger than a typical slip distance, when faults are not perfectly planar surfaces. Geometric resistance has received little attention in the literature, but our analysis suggests it may be substantially larger than frictional resistance on many faults.

[3] The classic estimate of the average background shear stress, τ^b, on an active fault is the product of a Byerlee friction coefficient ∼0.6–0.9 [*Byerlee*, 1978] and an effective normal stress, σ^{eff}, calculated assuming hydrostatic pore pressure. Yet many lines of evidence [see *Noda et al.*, 2009, and references therein] suggest that major plate-boundary faults, such as the San Andreas Fault (SAF), are exceptionally weak, in the sense that they host earthquakes at values of $\tau^b/\sigma^{\mathrm{eff}}$ far less than those predicted by Byerlee's law and hydrostatic pore pressure. For example, *Noda et al.* [2009, Figure 8] show that measurements of the principal stress orientation near the SAF [*Townend and Zoback*, 2004], together with basic assumptions about the strength of the surrounding medium, require $\tau^b/\sigma^{\mathrm{eff}} < 0.3$ on the SAF. That constraint is consistent with the directly measured value of $\tau^b/\sigma^{\mathrm{eff}} = 0.21$ at the bottom of the San Andreas Fault Observatory at Depth pilot hole at 2.1 km depth [*Hickman and Zoback*, 2004].

[4] Several theories have been proposed to explain why mature faults like the SAF operate at very low $\tau^b/\sigma^{\mathrm{eff}}$ levels. One possibility is a greatly reduced effective normal stress σ^{eff} due to the presence of near-lithostatic pore fluid pressure within fault zones [*Byerlee*, 1990; *Rice*, 1992; *Faulkner and Rutter*, 2001]. That explanation does not seem likely, at least for crustal faults, as measurements of pore pressure within Earth's crust generally indicate hydrostatic conditions [*Townend and Zoback*, 2000], even in the SAF itself [*Zoback et al.*, 2010]. Other theories appeal to anomalously low frictional resistance, from either frictionally weak clay-rich materials [*Morrow et al.*, 2000; *Carpenter et al.*, 2011] or weak fault zone fabrics [*Collettini et al.*, 2009] at seismogenic depths. Weak materials occur within the creeping section of the SAF and appear to be the most likely explanation for its weakness, but that cannot explain the similarly low stresses on other seismogenic parts of the SAF. The leading explanation for the weakness of faults which accommodate deformation through earthquakes, rather than creep, is the coseismic activation of dynamic weakening mechanisms such as thermal pressurization and flash heating [*Rice*, 2006; *Noda et al.*, 2009] that dramatically reduce frictional resistance during earthquake slip.

[5] Extreme dynamic weakening at coseismic slip rates has been widely observed in high-velocity friction experiments [e.g., *Tsutsumi and Shimamotom*, 1997; *Di Toro et al.*, 2004; *Hirose and Shimamoto*, 2005; *Beeler et al.*, 2008; *Goldsby and Tullis*, 2011; *Di Toro et al.*, 2011]. Planar faults governed by strongly rate-weakening friction laws support self-sustaining slip-pulse ruptures at background stress levels τ^b around a critical stress level $\tau^{\mathrm{pulse}} \approx 0.25\sigma^{\mathrm{eff}}$ [*Cochard and Madariaga*, 1996; *Beeler and Tullis*, 1996; *Zheng and Rice*, 1998; *Lapusta and Rice*, 2003; *Lykotrafitis et al.*, 2006; *Noda et al.*, 2009], even with off-fault plasticity [*Dunham et al.*, 2011a; *Gabriel et al.*, 2013]. Given that

dynamic weakening is so ubiquitous in friction experiments, and that dynamic weakening permits self-sustaining rupture at very low background stress levels, one might expect to find deviatioric stresses in the crust equal to about 0.2 or 0.3 times the effective normal stress. However, this is not observed. Instead, across many different tectonic regions around the world, stresses are largely consistent with a critically stressed crust having ratios of shear to effective normal stress consistent with Byerlee's law ($\tau^b/\sigma^{\mathrm{eff}} \approx 0.6$–0.9) [see *Townend and Zoback*, 2000, and references therein].

[6] Additional evidence supporting fault operation at stress levels compatible with Byerlee's law comes from the observed range of dip angles of seismically active normal and thrust faults. Many of these faults are not optimally oriented in the present-day stress regime and have been reactivated. By assuming that faulting occurs at constant $\tau^b/\sigma^{\mathrm{eff}}$ and that off-fault material strength is limited by a constant internal friction coefficient, *Sibson* [1985] placed bounds on the range of dip angles permitting fault reactivation. In particular, he showed there exists a lock-up angle beyond which faults become so severely misoriented that no slip can occur on them. Because the lock-up angle depends on the critical $\tau^b/\sigma^{\mathrm{eff}}$ for rupture, measurements of lock-up angle can be used to estimate that $\tau^b/\sigma^{\mathrm{eff}}$. This has been done using compilations of dip angles of seismically active dip-slip faults [*Sibson*, 1994; *Sibson and Xie*, 1998; *Collettini and Sibson*, 2001], revealing a general agreement with Byerlee-level ratios of shear to effective normal stress.

[7] In light of the above discussion, our challenge is to reconcile the relatively high stress levels observed on all but the most mature plate-boundary faults with the ubiquitous occurrence of dynamic weakening at coseismic slip rates, which ought to permit faulting at much lower stress levels. The simplest explanation is that dynamic weakening is unique to mature faults having well-developed ultracataclastic fault cores that permit the extreme strain localization required for concentrated shear heating and activation of thermal weakening mechanisms [*Rice*, 2006]. This is certainly a possibility that cannot be dismissed, and it could be tested by measurements of shear-zone width and heat production. But we see an alternative explanation, in which coseismic frictional resistance is extremely low on all faults.

[8] Our basic premise is that the elevated τ^b on most faults arises from an additional shear resistance to slip, beyond frictional resistance, offered by complex fault geometry. There are many forms of geometric complexity, ranging from roughness of a single fault surface to compound failure, in a single event, of multiple fault segments or strands linked by damaged rock in step-overs. Slip in such systems, unlike slip on an infinitely long planar fault, cannot be accomodated without straining the material directly adjacent to geometric irregularities. Associated with those strains are restoring stresses, some of which oppose the overall sense of slip. These stresses are ultimately bounded by the finite strength of the rock, with further deformation involving inelastic processes and energy dissipation during plastic flow.

[9] In the remainder of this work, we study this additional geometric resistance for the specific case of band-limited self-similar fractal faults having roughness at all scales above a minimum roughness wavelength. We term this additional resistance "roughness drag" and quantify its

importance through both analytical solutions and dynamic rupture simulations.

1.1. Field and Laboratory Measurements of Fault Roughness

[10] We begin by reviewing field and laboratory measurements of fault roughness and then discuss how it affects fault mechanics. *Anderson* [1951] recognized that natural fault surfaces are not planar but irregular at all scales. Early measurements by *Brown and Scholz* [1985], *Power and Tullis* [1988, 1991, 1995], and *Lee and Bruhn* [1996] concluded that natural fault surfaces are self-similar fractals, in the sense that root-mean-square (RMS) height fluctuations are proportional to profile length.

[11] To be more precise, consider a one-dimensional fault profile $y = h(x)$ having zero mean. The RMS roughness contribution from wavenumbers k between k_{min} and k_{max} is

$$h_{RMS}(k_{min}, k_{max}) = \sqrt{\frac{1}{\pi} \int_{k_{min}}^{k_{max}} P_h(k) dk}, \qquad (1)$$

where $P_h(k)$ is the power spectral density of $h(x)$. Self-similar faults have

$$P_h(k) = (2\pi)^3 \alpha^2 |k|^{-3}, \qquad (2)$$

in which α is the amplitude-to-wavelength ratio, which controls the severity of deviations from planarity. Roughness is dominated by the longest wavelengths, and if we take $k_{min} = 2\pi/L$ and $k_{max} \to \infty$, then $h_{RMS} = \alpha L$. Additional mathematical details are given by *Dunham et al.* [2011b].

[12] Roughness in the slip-parallel direction (the direction of interest in this study) is characterized by $\alpha \sim 10^{-3}$ to 10^{-2} [*Power and Tullis*, 1991]. Some studies indicate that roughness decreases with cumulative slip as faults mature before ultimately leveling off [*Sagy and Brodsky*, 2009; *Brodsky et al.*, 2011]. *Candela et al.* [2012] speculate that the terminal roughness level reflects a balance between wear processes acting to smooth the fault and roughening processes. The latter could include the tendency for dynamic ruptures to branch away from their current propagation direction at high speeds [*Poliakov et al.*, 2002; *Rice et al.*, 2005].

[13] Many recent studies [*Renard et al.*, 2006; *Sagy et al.*, 2007; *Sagy and Brodsky*, 2009; *Candela et al.*, 2009, 2011, 2012; *Brodsky et al.*, 2011; *Bistacchi et al.*, 2011] have provided high resolution measurements of fault roughness, using a variety of techniques including analysis of surface traces at the largest scales, over nine orders of magnitude in length. Measurements using a single technique or instrument, which are necessarily limited in bandwidth, suggest that fault surfaces are more likely to be self-affine rather than self-similar, with a Hurst exponent $H \approx 0.8$ in the slip-parallel direction. However, as pointed out by *Shi and Day* [2013], the data set as a whole is well fitted by a single self-similar power spectral density function (for which $H = 1$). We concur and therefore focus our discussion and analysis on self-similar faults.

1.2. Effects of Roughness on Fault Mechanics

[14] Several studies have examined how deviations from planarity influence fault mechanics. Slip on rough faults perturbs the stress field in the vicinity of the fault, most substantially over an off-fault distance proportional to the wavelength of roughness considered. These stress changes were first quantified using a linearized boundary perturbation analysis of quasi-static slip on frictionless sinusoidal faults by *Saucier et al.* [1992]. Those authors pointed out that the near-fault stress field has a rather complex pattern that can differ significantly from the regional stress field. They suggested nonplanarity as a possible explanation for the unexpected orientations of the principal stresses near the SAF at the Cajon Pass borehole. That sinusoidal fault analysis was subsequently extended to sliding at constant friction coefficient by *Chester and Chester* [2000], who also applied Mohr-Coulomb failure analysis to predict the locations and extent of regions in which the stress perturbations are likely to cause inelastic deformation and secondary faulting off the main fault.

[15] *Dunham et al.* [2011b] extended this boundary perturbation approach to fractal faults, finding that RMS stress perturbations, $\Delta\sigma_{RMS}$, on band-limited self-similar faults are dominated by the shortest roughness wavelengths:

$$\Delta\sigma_{RMS} = 2\pi^2 \alpha G^* \Delta/\lambda_{min}, \qquad (3)$$

for $G^* = G/(1-\nu)$, with shear modulus G and Poisson's ratio ν, slip Δ, and minimum roughness wavelength λ_{min}. The stress perturbations are simply the product of strains $\sim \alpha\Delta/\lambda_{min}$ and the elastic modulus. As equation (3) shows, these stress perturbations are an $O(\alpha)$ effect.

[16] When these $O(\alpha)$ stress perturbations are projected onto the nonplanar fault, an $O(\alpha^2)$ additional resistance to slip appears. The effect, which must be invariant to flipping the profile $y = h(x) \to y = -h(x)$, is necessarily $O(\alpha^2)$; the $O(\alpha)$ traction perturbations introduce no net resistance once averaged over the zero-mean fault profile. A similar resistance arises during the sliding of glaciers and ice sheets over rough beds [*Nye*, 1969, 1970]. *Dieterich and Smith* [2009] were the first to recognize the importance of this effect for faulting; they called it the back stress, though in this study we adopt the more specific term "roughness drag," denoted as τ^{drag}. Using a two-dimensional static, linear elastic boundary element model with constant friction coefficient, *Dieterich and Smith* [2009] found that roughness reduces fault slip below that occurring on planar faults. They proposed that the otherwise ever-growing roughness-induced stress perturbations are instead relaxed via brittle failure processes (off-fault seismicity and secondary faulting) within the off-fault material. They also showed that the proposed rates of stress relaxation with distance from faults follow a power law that is consistent with the observed decay rate of background seismicity with distance from faults.

[17] The first part of our present study is a rigorous derivation of the roughness drag effect. This is done within the simplifying assumptions of quasi-static, ideally elastic off-fault response and frictionless sliding; the latter only serves to highlight that this resistance is entirely distinct from frictional resistance. We confirm the scaling arguments of *Dieterich and Smith* [2009] that $\tau^{drag} \sim \alpha^2 G^* \Delta/\lambda_{min}$ and obtain a precise expression for τ^{drag} with the proper dimensionless prefactor. Given that the amplitude-to-wavelength ratio α varies over an order of magnitude in nature and that $\tau^{drag} \propto \alpha^2$, we expect substantial differences in τ^{drag} for faults of varying degrees of structural maturity or roughness.

This leads us to propose the following self-consistent explanation of why mature and immature faults operate at distinctly different background stress levels. We assume that dynamic weakening occurs on all faults, so that frictional resistance and heat production during earthquakes is low for both mature and immature faults. We hypothesize that the background stress level, τ^b, required for rough faults to host earthquakes is approximately equal to the combined resistance from friction and geometric irregularities: $\tau^b \approx \tau^{\text{pulse}} + \tau^{\text{drag}}$. This implies two extreme scenarios. For smooth faults, $\tau^{\text{drag}} \ll \tau^{\text{pulse}}$ so that $\tau^b \approx \tau^{\text{pulse}} \approx 0.25\sigma^{\text{eff}}$. For rough faults, the much larger τ^{drag} raises τ^b to a level substantially higher than τ^{pulse}. We expect that the finite strength of the off-fault material ultimately bounds τ^b to a value determined by the internal friction of the material. In that case, we expect $\tau^b/\sigma^{\text{eff}}$ to be in the range of 0.6 to 0.9, consistent with Byerlee's law, but with the important distinction that this value has little or no relation to the friction coefficient on the fault itself and should certainly not be identified as the static friction coefficient. We support this idea using simulations of dynamic ruptures on rough faults.

2. Roughness Drag

[18] In this section, we quantify the additional resistance to sliding from self-similar roughness of a fault surface. We restrict attention to roughness at scales larger than slip in a single event, with shorter wavelength roughness (i.e., down to asperity contact or grain scales) contributing to the frictional resistance. We assume two-dimensional plane strain deformation, ideally elastic off-fault response, and frictionless sliding along an infinitely long fault. We employ the boundary perturbation technique used by *Saucier et al.* [1992], *Chester and Chester* [2000], and *Dunham et al.* [2011b], but we extend it to second order in the small parameter α. The analysis yields the $O(\alpha)$ and $O(\alpha^2)$ perturbations in displacement and stress fields about a given solution for a planar fault. This unperturbed solution is simply constant slip Δ, in the x direction, across a planar fault $y = 0$ between two half-spaces having uniform stresses σ_{ij}^0. Neglecting friction dramatically simplifies the analysis and facilitates greater insight into the physical nature of roughness drag.

[19] Roughness induces tractions $T(x)$ in the x direction that oppose the sense of slip. We define the roughness drag as the expectation value of those tractions, in excess of the shear traction in the unperturbed solution:

$$\tau^{\text{drag}} = E[T(x) - \sigma_{xy}^0], \qquad (4)$$

where $E[\cdot]$ denotes expectation value or ensemble average over a population of rough faults and σ_{xy}^0 is the background shear stress in the unperturbed problem. Because we assume frictionless sliding, $\sigma_{xy}^0 = 0$ in our analysis, though for sliding at constant friction coefficient f, $\sigma_{xy}^0 = f(-\sigma_{yy}^0)$ is the frictional resistance. We find

$$\tau^{\text{drag}} = 8\pi^3 \alpha^2 G^* \Delta/\lambda_{\text{min}}. \qquad (5)$$

A detailed derivation, including a precise definition of $T(x)$, is given in Appendix A.

[20] Taking $G^* = 40$ GPa yields

$$\tau^{\text{drag}} \approx 10 \text{ MPa} \left(\frac{\alpha}{10^{-3}}\right)^2 \left(\frac{\Delta}{\lambda_{\text{min}}}\right). \qquad (6)$$

Comparing to the RMS stress perturbations $\Delta\sigma_{\text{RMS}}$ given by equation (3), we see that $\tau^{\text{drag}} = 4\pi\alpha\Delta\sigma_{\text{RMS}}$. We expect these expressions to become inaccurate when any of the model assumptions, specifically ideally elastic off-fault response or no fault opening, are violated.

[21] If we consider roughness wavelengths down to the scale of slip ($\Delta/\lambda_{\text{min}} \to 1$) and take $\sigma^{\text{eff}} \approx 100$ MPa as representative of conditions at seismogenic depths, our estimate of τ^{drag} in equation (6) suggests that $\tau^{\text{drag}}/\sigma^{\text{eff}} \sim 0.1$ for $\alpha \sim 10^{-3}$, and that it increases to substantially higher values for rougher faults with larger α.

3. Rupture Propagation on Rough Faults

3.1. Model Description

[22] The perturbation analysis described in the previous section suggests that roughness drag plays an important role in the faulting process, on all but the smoothest faults in nature. However, that analysis assumes quasi-static, ideally elastic deformation with frictionless sliding. In this section, we relax those assumptions in fully dynamic earthquake rupture simulations. We use a two-dimensional plane strain model that incorporates strongly rate-weakening friction on the fault and Drucker-Prager viscoplasticity to account for inelastic deformation of the off-fault material. Detailed descriptions of friction, plasticity, and material parameters can be found in *Dunham et al.* [2011a, 2011b]; the numerical method (a high-order finite difference method) is described in *Dunham et al.* [2011a] and *Kozdon et al.* [2011, 2012].

[23] Here we only summarize details that are immediately relevant to the current study. Fault friction obeys a rate-and-state law that features the direct effect and evolution, over a characteristic slip distance, toward a strongly velocity-weakening steady state. Such laws give rise to self-healing slip pulses when the background shear stress, τ^b, is sufficiently low (specifically around τ^{pulse} on a flat fault in an elastic medium) [*Zheng and Rice*, 1998]. The surrounding material is described by an elastic-viscoplastic Drucker-Prager rheology without cohesion, which avoids pathological growth of stress at geometric irregularities and prevents fault opening [*Dunham et al.*, 2011b].

[24] Figure 1a illustrates the main features of our model. The medium is homogeneous and infinite in extent. The fault is a band-limited self-similar profile $y = h(x)$, generated by filtering random Gaussian white noise to obtain the desired power spectral density function given by equation (2). We restrict roughness wavelengths to those between $\lambda_{\text{min}} = 30\Delta x$ and fault profile length L, where Δx is the grid spacing. We choose $L = 60$ km, $\lambda_{\text{min}} = 300$ m, and $\Delta x = 10$ m, which is sufficient to demonstrate the importance of roughness drag on faults with $\alpha \sim 10^{-2}$ while retaining enough computational efficiency to perform over a thousand simulations for the purpose of ensemble averaging.

[25] The uniform initial stress field, σ_{ij}^0, is specified in terms of the initial shear and effective normal stresses on $y = 0$, $\tau^b = -\sigma_{yx}^0$, and $\sigma^0 = -\sigma_{yy}^0$, and the angle Ψ between the maximum compressive principal stress and $y = 0$. Fault nonplanarity introduces spatial variability of the local shear
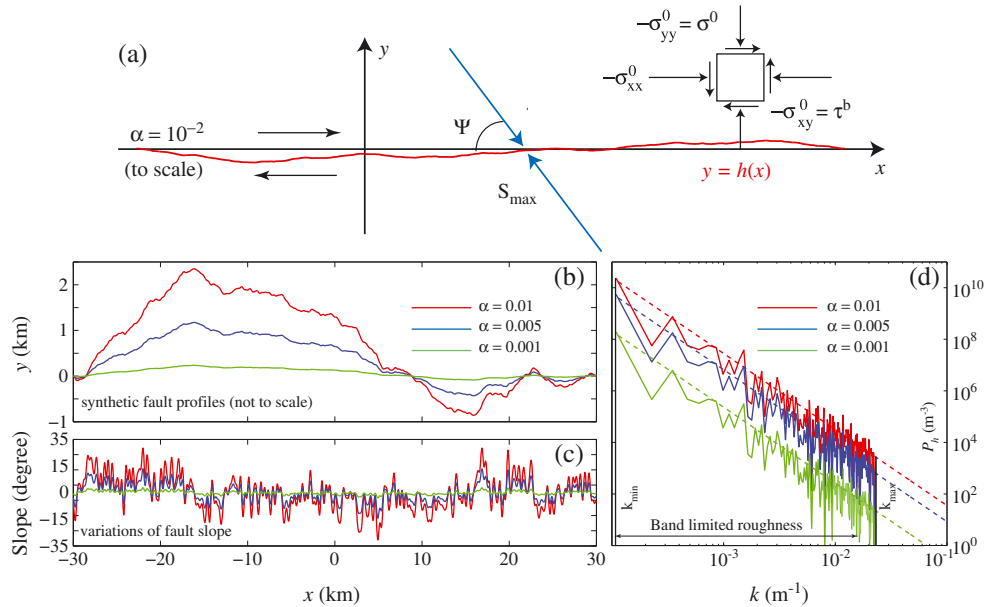
Figure 1. (a) Plane strain model with right-lateral slip on a band-limited self-similar fault with $\alpha = 10^{-2}$. The medium is loaded with a spatially uniform stress state, with the maximum principal stress inclined at an angle $\Psi = 50°$ to the fault. (b) Examples of synthetic self-similar fault profiles with $\alpha = 0.001$, 0.005, and 0.01. Fault length is $L = 60$ km and the minimum wavelength of roughness is $\lambda_{min} = 300$ m. (c) Variations of fault slope for the three examples. (d) Power spectral density of the three examples. Roughness is band-limited and has wavelengths between λ_{min} and L.

and normal tractions on the fault, τ and σ, as well as their ratio τ/σ (see Figure 2b). We neglect poroelastic effects.

[26] Ruptures are initiated by applying a localized stress perturbation at the desired hypocenter location. The simplest choice would be to randomly assign this location, but we do not expect that to be representative of natural events. Instead, nucleation seems most likely at locations with elevated values of τ/σ. However, it is well known that earthquakes nucleate over a finite region, rather than from a single point, and that region must be larger than a critical nucleation size, h^* [*Dieterich*, 1992; *Rice*, 1993; *Rubin and Ampuero*, 2005; *Fang et al.*, 2010]. For our model parameters, $h^* \sim 10^2$ m. Therefore, we smooth τ/σ to remove short-wavelength variations and select the nucleation location as the site of the highest smoothed τ/σ. We shift the profile to place the center of the nucleation zone at $x = 0$ (see Figures 2 and 3). With this procedure, nucleation most often occurs within major

extensional bends at which τ/σ is high due to the local fault orientation with respect to the background stress field.

3.2. Simulation Results

[27] In contrast to previous studies of ruptures on non-planar faults [*Dunham et al.*, 2011b; *Shi and Day*, 2013], which restricted attention to a few simulations, we model over a thousand ruptures with many different realizations of the random fault geometry. In this way, we can frame our discussion in terms of the statistical properties of the rupture process, specifically, the probability that rupture length exceeds a certain distance given values of τ^b/σ^0 and α. This approach is necessitated by the remarkable variability that emerges from individual realizations of the random geometry (Figure 3). Unlike the situation for planar faults [e.g., *Zheng and Rice*, 1998], there is no unique level of τ^b at which self-sustaining rupture first becomes possible.
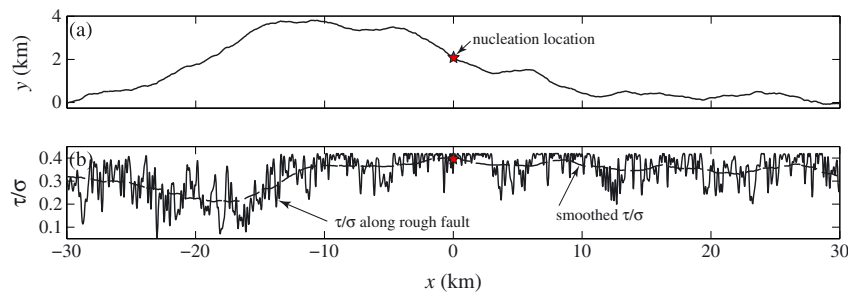

Figure 2. (a) Synthetic fault profile with $\alpha = 0.01$. (b) Initial shear to effective normal stress ratio τ/σ on the fault (solid line), obtained by resolving a uniform background stress onto the fault plane. Rupture is initiated by applying a stress perturbation at the location that has the largest smoothed τ/σ (dashed line), and the profile is shifted so that this location is at $x = 0$.
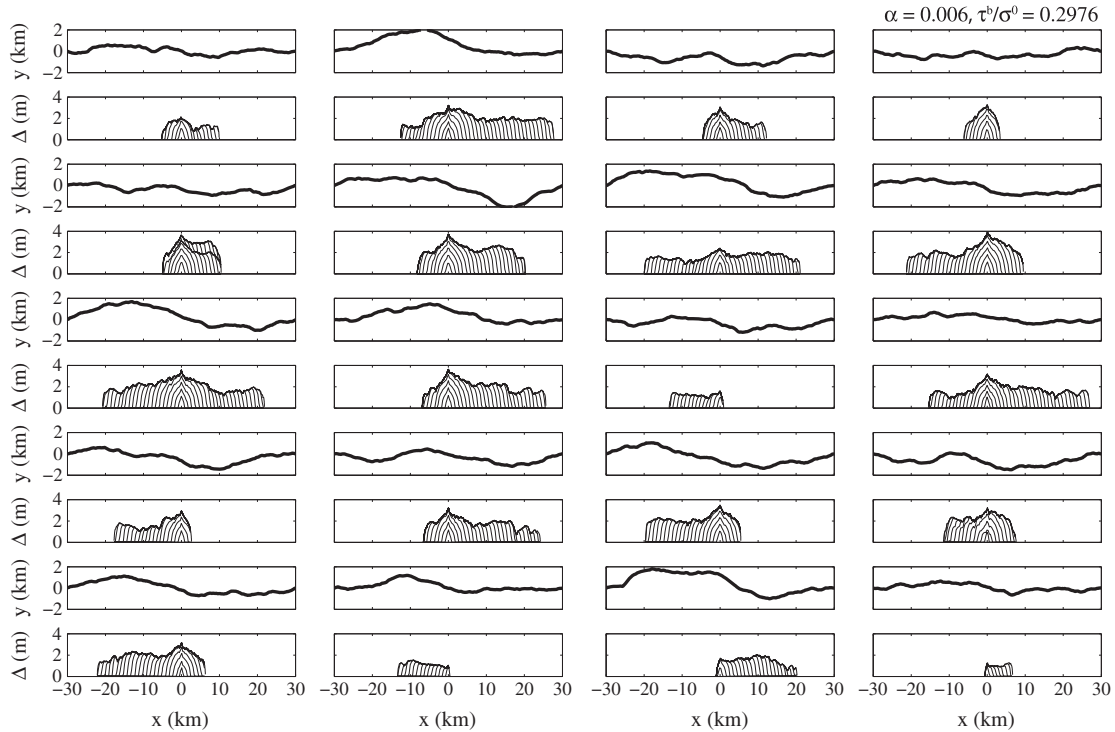
Figure 3. Ruptures on 20 randomly generated faults with $\alpha = 0.006$. All the simulations assume the same uniform initial stress state in the medium with $\tau^b = 37.5$ MPa, $\sigma^0 = 126$ MPa, and $\Psi = 50°$. The top panel for each case shows the fault profile while the bottom panel shows sequences of cumulative fault slip Δ every 0.28 s. Ruptures vary significantly in extent and slip distribution, illustrating the remarkable sensitivity of the rupture process to the detailed fault geometry.

[28] We also point out that the nonplanar geometry provides a realistic mechanism for rupture arrest. Indeed, most ruptures in our simulations stop naturally when they encounter unfavorable stress conditions (typically at compressional bends, where the local τ/σ is low). Some do reach the end of the computational domain, but we speculate that with larger domains, even those ruptures would ultimately spontaneously arrest.

[29] This pronounced sensitivity to local fault conditions offers a potential explanation for the difficulty of predicting the occurrence of individual earthquakes based on a threshold stress level, as in the time-predictable recurrence model [*Shimazaki and Nakata*, 1980]. For example, by the early 1990s, stresses in the hypocentral region of the 1966 M_w 6.0 Parkfield, California, earthquake had arguably reached levels commensurate with those in 1966 [*Murray and Segall*, 2002]. Yet three events (M_w 4.3, 4.6, and 4.7) in 1992–1994, all close to the 1966 hypocenter, failed to grow into the expected M_w 6.0 event. Similarly, the 2011 M_w 9.0 Tohoku-Oki, Japan, earthquake was preceded by 2 days by a M_w 7.3 foreshock only a few tens of kilometers from the hypocenter of the M_w 9.0 event [*Gusman et al.*, 2013].

[30] Despite the random nature of individual rupture histories on rough faults, we do observe a tendency for rupture lengths to increase at higher background stress levels (Figure 4). Figure 5 shows probability contour plots of rupture length as a function of background stress level τ^b/σ^0 for several different amplitude-to-wavelength ratios α. Rupture length is defined as the maximum propagation distance from the hypocenter in either direction. As expected, ruptures

propagate farther at higher background stresses (larger τ^b/σ^0) and on smoother faults (smaller α). In addition, roughness increases the variability in rupture extent. For example, on flat faults, there exists a critical τ^b/σ^0 below which ruptures immediately arrest and above which ruptures propagate indefinitely. This approximately corresponds to the vertical line at $\tau^b = \tau^{\text{pulse}}$ in Figure 5, though the critical stress level when accounting for off-fault plasticity is
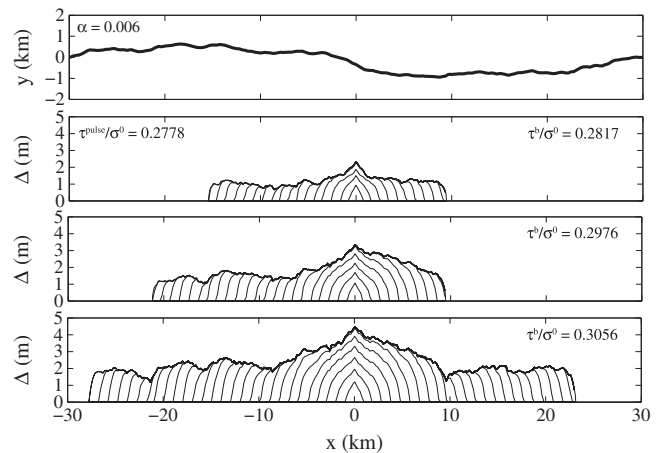

Figure 4. Sequences of cumulative slip Δ every 0.28 s for ruptures occurring on the same fault but at three different τ^b levels. The extent of rupture and the amount of fault slip increase with background stress.
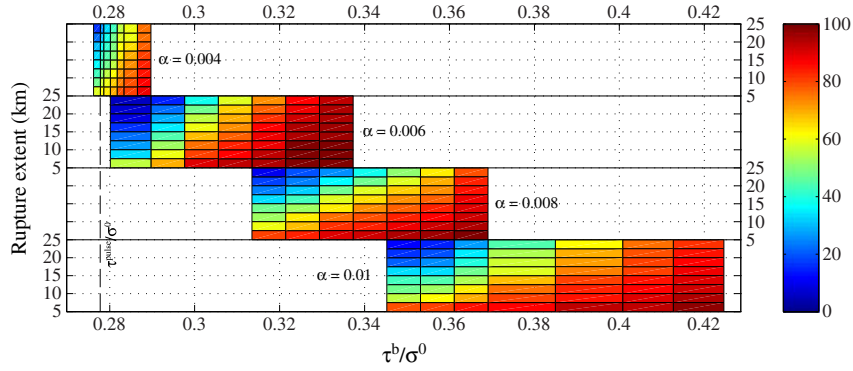
Figure 5. Percentage of ruptures exceeding a given spatial extent, as a function of background stress level τ^b/σ^0; shown for four values of amplitude-to-wavelength ratio α. On average, rupture extent increases with τ^b/σ^0 for fixed α, and rougher faults with larger α require larger τ^b/σ^0 to attain the same propagation distance.

slightly higher than τ^{pulse} [*Dunham et al.*, 2011a; *Gabriel et al.*, 2013]. There is also some sensitivity of this critical stress level to the nucleation process: *Gabriel et al.* [2012] have demonstrated the possibility of self-sustaining slip pulses at stress levels below τ^{pulse} when rupture growth is initially forced over some region much larger than the minimum nucleation length. Such conditions do not arise in our simulations. When faults are rough, there emerges a finite range of rupture lengths at a given τ^b/σ^0 and α, with the level of variability increasing as α increases. These general points are also illustrated in Figure 6, which shows the percentage of ruptures exceeding 20 km as a function of τ^b/σ^0 and α.

[31] The results illustrated in Figures 5 and 6 lend qualitative support to our hypothesis that even if dynamic weakening acts on all faults, structurally complex faults require higher τ^b levels to host earthquakes because of roughness drag. To quantitatively assess the role of roughness drag, we determine τ^b/σ^0 levels at which 50%, 60%, 70%, and 80% of ruptures exceed 20 km extent (Figure 7). We also plot background stress levels predicted by our analysis, assuming $\tau^b \approx \tau^{\text{pulse}} + \tau^{\text{drag}}$, with average fault slip values chosen
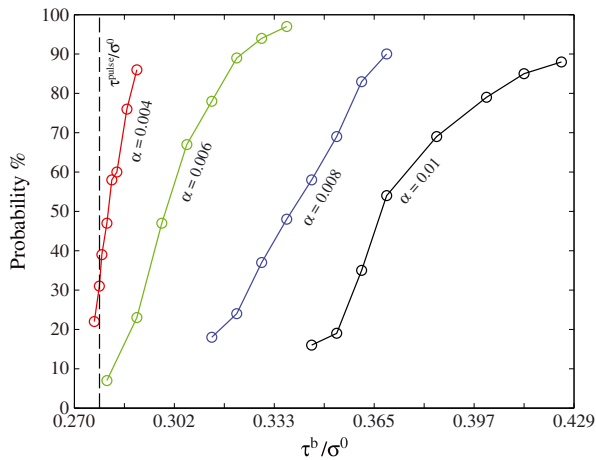
between 2 and 5 m to encompass the range emerging in our simulations. The overall trend of the simulation results falls within the range of stress levels suggested by the perturbation analysis. We note that even with the restricted range of roughness wavelengths included in the model (down to only $\lambda_{\min}/\Delta \sim 100$), the background stress level on the roughest faults ($\alpha = 10^{-2}$) is about 1.5 times larger than on a flat fault.

4. Discussion

[32] Our numerical results indicate that, at least for the range of roughness wavelengths studied, the stress level at which faults host moderate to large earthquakes is the sum of τ^{pulse} and τ^{drag}. As discussed in section 1, this potentially provides a self-consistent explanation for the difference in the observed background stress levels on mature and immature faults. However, for the range of roughness wavelengths captured in our simulations, τ^b is only increased to an intermediate level of about $0.4\sigma^0$ (Figure 7). To rigorously quantify the importance of roughness drag requires simulations capable of resolving roughness wavelengths down
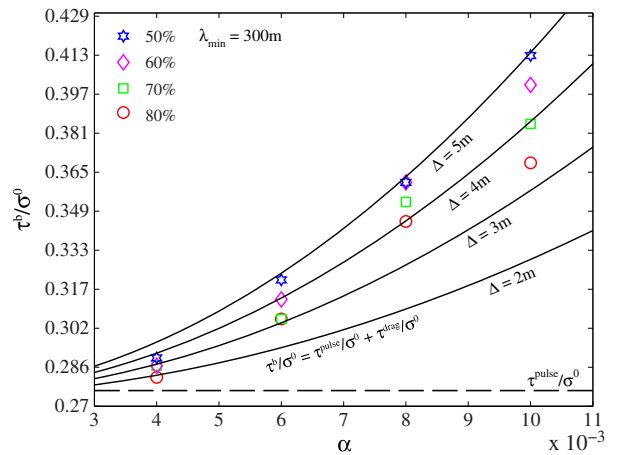

Figure 6. Probabilities of rupture to reach an extent of 20 km (in either direction) from the hypocenter as a function of background stress level τ^b. Rougher faults require larger τ^b to reach the same extent.

Figure 7. Background stress levels τ^b required for 50%, 60%, 70%, and 80% of ruptures to propagate beyond 20 km in at least one direction. Solid lines are predictions using the theoretical expression for roughness drag in equation (5).
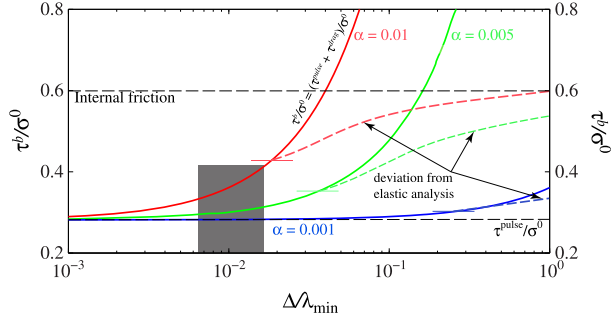
Figure 8. Background stress level τ^b/σ^0 as a function of $\Delta/\lambda_{\min}$ according to the hypothesis that $\tau^b/\sigma^0 = (\tau^{\text{pulse}} + \tau^{\text{drag}})/\sigma^0$, with roughness drag given by equation (5) (solid lines). The shaded area covers the parameter space investigated in the current study. The onset of pervasive off-fault plasticity is expected to saturate τ^b/σ^0 at a level determined by the internal friction coefficient of the surrounding material (shown schematically with dashed lines).

to the scale of slip. That would mean increasing the number of grid points resolving the domain by over an order of magnitude in each direction; such simulations are presently beyond our computational capabilities but are targets for future work.

[33] Nonetheless, we offer the following speculation. By combining our theoretical expression for roughness drag (equations 5 and 6) with our hypothesis that the critical stress level is $\tau^b \approx \tau^{\text{pulse}} + \tau^{\text{drag}}$, we obtain a prediction of τ^b as a function of $\Delta/\lambda_{\min}$. This is shown in Figure 8 for several values of α (solid lines). The shaded region indicates the approximate range of $\Delta/\lambda_{\min}$ covered by our current simulations, for which $\Delta/\lambda_{\min} \sim 0.01$. Our prediction will break down as $\Delta/\lambda_{\min} \to 1$ due to the occurrence of pervasive off-fault yielding, and we expect that τ^b/σ^0 will ultimately saturate at a level determined by the finite strength of the off-fault material. For a fractured rock mass obeying a Drucker-Prager or Mohr-Coulomb type failure criterion, we expect this level to be around the internal friction coefficient of the material. We have indicated this schematically in Figure 8 with dashed lines. Our analysis also suggests that for very rough faults ($\alpha \sim 10^{-2}$), it is only necessary to include roughness wavelengths down to $\sim$100 m to begin to approach the expected saturation level $\tau^b \approx 0.6\sigma^0$. This is within reach of current computations, but is beyond the scope of this initial study.

[34] Figure 8 also shows that roughness drag is likely to be the dominant resistance mechanism on all but the smoothest faults. Only for $\alpha \sim 10^{-3}$ does roughness drag remain negligible compared to frictional resistance in the $\Delta/\lambda_{\min} \to 1$ limit. Thus, only the most structurally mature faults are expected to operate at the very low background stress levels predicted by studies of dynamic weakening on planar faults [*Noda et al.*, 2009], even when dynamic weakening occurs on all faults.

[35] Our results have interesting implications for geomechanics. The Coulomb failure criterion with Byerlee friction coefficients is the standard rule of thumb in predicting whether or not nonoptimally oriented faults can be reactivated in the present-day stress regime [e.g., *Sibson*, 1985; *Jaeger et al.*, 2007]. Such methods are widely applied in the

energy and mining industry and perform remarkably well in practice [e.g., *Hennings et al.*, 2012]. It is tempting to identify the ratio of shear to effective normal stress governing fault operation with a "friction coefficient," as is routinely done within the literature. Yet our study suggests that this interpretation is incorrect. The actual frictional resistance to slip can be dramatically lower than predicted by Byerlee's law (or even zero), and faults are still expected to become capable of hosting earthquakes only when $\tau^b \approx 0.6\sigma^0$ due to the additional resistance to slip arising from geometric irregularities.

[36] Furthermore, although this study has focused on rupture dynamics on a single continuous self-similar fault surface in two dimensions, we expect our ideas carry over to three-dimensional fault networks characterized by other types of geometric complexity, for example, en echelon fault segments. In that case, we expect that the background stress level required for through-going rupture would be determined by the material strength of the step-over regions between the individual segments rather than the frictional strength of the segments themselves.

5. Conclusions

[37] Motivated by observations that mature and immature faults host earthquakes at distinctly different levels of background shear stress, we investigated how geometric complexity of the fault affects the stress levels at which faults operate. This was done in the idealization of self-similar fractal fault surfaces characterized in terms of the amplitude-to-wavelength ratio of roughness, α. Natural faults have values of α ranging from 10^{-3} to 10^{-2}, depending on the degree of structural maturity. Through an $O(\alpha^2)$ boundary perturbation analysis, we identified an additional resistance to slip from fault roughness that acts in addition to the frictional resistance. Estimates of this roughness drag, τ^{drag}, suggest that it is the dominant source of resistance in earthquakes on all but the smoothest naturally occurring faults. This is particularly true if faults undergo the extreme coseismic weakening that is ubiquitous in high-velocity rock friction experiments. We derived an explicit expression for τ^{drag} and tested its validity with dynamic rupture simulations employing strongly rate-weakening fault friction and off-fault plasticity. The predicted expressions for overall resistance were found to be generally consistent with the background stress level that permits the occurrence of moderate to large earthquakes on rough faults. Further, higher resolution simulations of ruptures on faults having roughness wavelengths approaching the scale of slip are required to fully test our ideas. Nonetheless, the simultaneous existence of dynamic weakening and roughness drag provides a self-consistent understanding of crustal stress levels, fault reactivation theory, negligible heat production from earthquakes, and the extremely low-stress operation of major plate-boundary faults.

Appendix A: Boundary Perturbation Analysis of Roughness-Induced Shear Resistance

[38] In this Appendix, we calculate the perturbations in displacement and stress arising from fault roughness during quasi-static frictionless sliding. Then, for the specific case of band-limited self-similar roughness, we derive an

expression for the roughness-induced shear resistance or roughness drag. The analysis employs the boundary perturbation technique used by *Chester and Chester* [2000] and *Dunham et al.* [2011b]. Like those authors, we focus on two-dimensional, static, plane strain deformation in an infinite elastic medium. A similar calculation was performed for glacier sliding by *Nye* [1969, 1970].

[39] Assuming small deviations from planarity, the fault profile $y = h(x)$ and slope $m(x) = h'(x)$ can be written as $h(x) = \epsilon \tilde{h}(x)$ and $m(x) = \epsilon \tilde{m}(x)$ for some dimensionless, positive scalar ϵ. For a self-similar fault, we can identify the amplitude-to-wavelength ratio α as ϵ. Assuming that $\epsilon \ll 1$, we seek a series solution for the displacement and stress fields, $u_i(x,y)$ and $\sigma_{ij}(x,y)$, respectively, in powers of ϵ:

$$u_i(x,y) = u_i^{(0)}(x,y) + \epsilon u_i^{(1)}(x,y) + \epsilon^2 u_i^{(2)}(x,y) + O(\epsilon^3), \quad (A1)$$

$$\sigma_{ij}(x,y) = \sigma_{ij}^{(0)}(x,y) + \epsilon \sigma_{ij}^{(1)}(x,y) + \epsilon^2 \sigma_{ij}^{(2)}(x,y) + O(\epsilon^3). \quad (A2)$$

The zeroth-order terms correspond to the solution for a planar fault. For notational convenience, we write the first- and second-order terms as

$$\hat{u}_i(x,y) = \epsilon u_i^{(1)}(x,y), \quad \hat{\sigma}_{ij}(x,y) = \epsilon \sigma_{ij}^{(1)}(x,y), \quad (A3)$$

$$\check{u}_i(x,y) = \epsilon^2 u_i^{(2)}(x,y), \quad \check{\sigma}_{ij}(x,y) = \epsilon^2 \sigma_{ij}^{(2)}(x,y). \quad (A4)$$

[40] Given a boundary value problem involving interface conditions applied on the nonplanar fault $y = h(x)$, the boundary perturbation approach provides a method to successively calculate the $O(\epsilon)$, $O(\epsilon^2)$, etc., terms in the expansions (A1) and (A2). The specific problem we address is that of frictionless slip. In the absence of roughness (i.e., for the unperturbed, or flat fault, problem), there is constant slip Δ in the x direction with a uniform stress state σ_{ij}^0 in the medium. Because the fault is frictionless, $\sigma_{yx}^0 = 0$. We have neglected friction for two reasons. First, this assumption dramatically simplifies the following analysis; second, dynamic weakening experiments suggest there is very little frictional resistance during coseismic slip. The principal stresses in the unperturbed problem are thus parallel and perpendicular to $y = 0$, and we define the differential stress as

$$\sigma_D = \sigma_{xx}^0 - \sigma_{yy}^0. \quad (A5)$$

[41] Nonplanarity of the fault perturbs the stress field in the vicinity of the fault and also generates fluctuations in slip along the fault and in tractions opposing slip. After obtaining general expressions for the first- and second-order field perturbations caused by arbitrary deviations from planarity, we focus on the special case of a self-similar fault described by the power-law power spectral density (2). We express the expectation value of various quantities (like tractions opposing slip) as wavenumber integrals involving the power spectral density function, which can then be evaluated to obtain expressions for roughness drag and other quantities.

A1. General Solution for Elastic Half-Spaces Coupled Across a Planar Interface

[42] The general principle of the boundary perturbation approach is to replace fault interface conditions applied on a nonplanar fault with more complicated, approximate interface conditions applied on the unperturbed surface $y = 0$. A new boundary value problem for an effectively flat

interface is thus obtained. This is done in subsequent sections, and here we begin by first deriving a general solution to the static equilibrium equations for two half-spaces separated by a planar interface $y = 0$. The solution is written in a way that permits application of arbitrary interface conditions. The equilibrium equations, assuming isotropic linear elasticity, are

$$2(1-\nu)u_{x,xx} + (1-2\nu)u_{x,yy} + u_{y,xy} = 0, \quad (A6)$$

$$(1-2\nu)u_{y,xx} + 2(1-\nu)u_{y,yy} + u_{x,xy} = 0, \quad (A7)$$

in which commas denote partial derivatives (e.g., $u_{y,x} = \partial u_y/\partial x$). The equations are solved by Fourier transforming along the x direction, defining $U_i(k,y) = \int_{-\infty}^{\infty} u_i(x,y)e^{-ikx}dx$. By solving the resulting ordinary differential equations in the y direction and discarding solutions that diverge as $y \to \pm\infty$, the interior displacements can be written in terms of those on the interface:

$$U_x^{\pm}(k,y) = -\frac{\pm|k|U_x^{\pm}(k,0) + ikU_y^{\pm}(k,0)}{3-4\nu}ye^{\mp|k|y} + U_x^{\pm}(k,0)e^{\mp|k|y}, \quad (A8)$$

$$U_y^{\pm}(k,y) = -\frac{ikU_x^{\pm}(k,0) \mp |k|U_y^{\pm}(k,0)}{3-4\nu}ye^{\mp|k|y} + U_y^{\pm}(k,0)e^{\mp|k|y}, \quad (A9)$$

in which the superscript $\pm$ designates fields in the upper and lower half-spaces, respectively, such that $U_i(k,y) = U_i^+(k,y)$ for $y > 0$ and $U_i(k,y) = U_i^-(k,y)$ for $y < 0$. This notational convention applies to other fields as well. Fourier transforming Hooke's law using $\Sigma_{ij}(k,y) = \int_{-\infty}^{\infty} \sigma_{ij}(x,y)e^{-ikx}dx$, and substituting the displacement solutions (A8) and (A9) yields the transformed stress components:

$$\frac{\Sigma_{xx}^{\pm}(k,y)}{2G} = \left[ik\frac{3-2\nu}{3-4\nu}U_x^{\pm}(k,0) \mp |k|\frac{2\nu}{3-4\nu}U_y^{\pm}(k,0)\right]e^{\mp|k|y}$$
$$+ \left[\mp\frac{ik|k|}{3-4\nu}U_x^{\pm}(k,0) + \frac{k^2}{3-4\nu}U_y^{\pm}(k,0)\right]ye^{\mp|k|y}, \quad (A10)$$

$$\frac{\Sigma_{yy}^{\pm}(k,y)}{2G} = \left[ik\frac{2\nu-1}{3-4\nu}U_x^{\pm}(k,0) \mp |k|\frac{2-2\nu}{3-4\nu}U_y^{\pm}(k,0)\right]e^{\mp|k|y}$$
$$- \left[\mp\frac{ik|k|}{3-4\nu}U_x^{\pm}(k,0) + \frac{k^2}{3-4\nu}U_y^{\pm}(k,0)\right]ye^{\mp|k|y}, \quad (A11)$$

$$\frac{\Sigma_{xy}^{\pm}(k,y)}{2G} = \left[|k|\frac{2-2\nu}{3-4\nu}U_x^{\pm}(k,0) + ik\frac{1-2\nu}{3-4\nu}U_y^{\pm}(k,0)\right]e^{\mp|k|y}$$
$$+ \left[\frac{k^2}{3-4\nu}U_x^{\pm}(k,0) \pm \frac{ik|k|}{3-4\nu}U_y^{\pm}(k,0)\right]ye^{\mp|k|y}, \quad (A12)$$

in which G is shear modulus and ν is Poisson's ratio.

A2. Boundary Perturbation Procedure

[43] We next use the boundary perturbation approach to replace interface conditions on the nonplanar interface $y = h(x)$ with approximate interface conditions on the plane $y = 0$. Denote the displacement discontinuity in the tangential and normal directions (i.e., fault slip and opening) across $y = h(x)$ as $\delta(x)$ and $\omega(x)$, and the shear and normal stresses on

the sides of the interface as $\tau^{\pm}(x)$ and $\sigma^{\pm}(x)$. Employing the small angle (i.e., small fault slope) approximation and dropping $O(\epsilon^3)$ terms, these can be written as

$$\delta(x) = [1 - m^2(x)/2][u_x(x, h(x)^+) - u_x(x, h(x)^-)]$$
$$+ m(x)[u_y(x, h(x)^+) - u_y(x, h(x)^-)], \quad (A13)$$

$$\omega(x) = [1 - m^2(x)/2][u_y(x, h(x)^+) - u_y(x, h(x)^-)]$$
$$- m(x)[u_x(x, h(x)^+) - u_x(x, h(x)^-)], \quad (A14)$$

$$\tau^{\pm}(x) = [1 - 2m^2(x)]\sigma_{xy}(x, h(x)^{\pm})$$
$$- m(x)[\sigma_{xx}(x, h(x)^{\pm}) - \sigma_{yy}(x, h(x)^{\pm})], \quad (A15)$$

$$\sigma^{\pm}(x) = -\sigma_{yy}(x, h(x)^{\pm}) + 2m(x)\sigma_{xy}(x, h(x)^{\pm})$$
$$- m^2(x)[\sigma_{xx}(x, h(x)^{\pm}) - \sigma_{yy}(x, h(x)^{\pm})]. \quad (A16)$$

Next, we use a Taylor series expansion to replace a field $g(x, y)$, evaluated on $y = h(x)$, with

$$g(x, h(x)) \approx g(x, 0) + h(x)\frac{\partial g}{\partial y}(x, 0) + \frac{h^2(x)}{2}\frac{\partial^2 g}{\partial y^2}(x, 0). \quad (A17)$$

As before, we have dropped $O(\epsilon^3)$ terms.

[44] We now combine these two approximations by using the Taylor expansion (A17) to evaluate all fields in equations (A13)–(A16) on $y = 0$ instead of $y = h(x)$. Then substitute the perturbation expansion, equations (A1) and (A2), into those expressions and drop $O(\epsilon^3)$ terms. The result is

$$\delta(x) = [u_x^{(0)}](x) + [\hat{u}_x](x) + [\check{u}_x](x)$$
$$+ h(x)[u_{x,y}^{(0)}](x) + h(x)[\hat{u}_{x,y}](x)$$
$$+ 0.5h^2(x)[u_{x,yy}^{(0)}](x) - 0.5m^2(x)[u_x^{(0)}](x)$$
$$+ m(x)[u_y^{(0)}](x) + m(x)[\hat{u}_y](x)$$
$$+ h(x)m(x)[u_{y,y}^{(0)}](x), \quad (A18)$$

$$\omega(x) = [u_y^{(0)}](x) + [\hat{u}_y](x) + [\check{u}_y](x)$$
$$+ h(x)[u_{y,y}^{(0)}](x) + h(x)[\hat{u}_{y,y}](x)$$
$$+ 0.5h^2(x)[u_{y,yy}^{(0)}](x) - 0.5m^2(x)[u_y^{(0)}](x)$$
$$- m(x)[\hat{u}_x](x) - m(x)[u_x^{(0)}](x)$$
$$- h(x)m(x)[u_{x,y}^{(0)}](x), \quad (A19)$$

$$\tau^{\pm}(x) = \sigma_{xy}^{(0)}(x, 0^{\pm}) + \hat{\sigma}_{xy}(x, 0^{\pm}) + \check{\sigma}_{xy}(x, 0^{\pm})$$
$$+ h(x)\sigma_{xy,y}^{(0)}(x, 0^{\pm}) + h(x)\hat{\sigma}_{xy,y}(x, 0^{\pm})$$
$$+ 0.5h^2(x)\sigma_{xy,yy}^{(0)}(x, 0^{\pm}) - 2m^2(x)\sigma_{xy}^{(0)}(x, 0^{\pm})$$
$$- h(x)m(x)[\sigma_{xx,y}^{(0)}(x, 0^{\pm}) - \sigma_{yy,y}^{(0)}(x, 0^{\pm})]$$
$$- m(x)[\sigma_{xx}^{(0)}(x, 0^{\pm}) - \sigma_{yy}^{(0)}(x, 0^{\pm})]$$
$$- m(x)[\hat{\sigma}_{xx}(x, 0^{\pm}) - \hat{\sigma}_{yy}(x, 0^{\pm})], \quad (A20)$$

$$\sigma^{\pm}(x) = -\sigma_{yy}^{(0)}(x, 0^{\pm}) - \hat{\sigma}_{yy}(x, 0^{\pm}) - \check{\sigma}_{yy}(x, 0^{\pm})$$
$$- h(x)\sigma_{yy,y}^{(0)}(x, 0^{\pm}) - h(x)\hat{\sigma}_{yy,y}(x, 0^{\pm})$$
$$+ 2h(x)m(x)\sigma_{xy,y}^{(0)}(x, 0^{\pm}) + 2m(x)\sigma_{xy}^{(0)}(x, 0^{\pm})$$
$$+ 2m(x)\hat{\sigma}_{xy}(x, 0^{\pm}) - 0.5h^2(x)\sigma_{yy,yy}^{(0)}(x, 0^{\pm})$$
$$- m^2(x)[\sigma_{xx}^{(0)}(x, 0^{\pm}) - \sigma_{yy}^{(0)}(x, 0^{\pm})]. \quad (A21)$$

We have introduced the simplifying notation for jumps in some field $g(x, y)$ across $y = 0$:

$$[g](x) = \lim_{\eta \to 0}[g(x, \eta) - g(x, -\eta)]; \quad (A22)$$

later, we employ a similar notation in the Fourier domain for some transformed field $G(k, y)$:

$$[G](k) = \lim_{\eta \to 0}[G(k, \eta) - G(k, -\eta)]. \quad (A23)$$

A3. Perturbations From Roughness

[45] Now consider the problem of quasi-static slip on a frictionless fault with no opening in the fault-normal direction. The specific interface conditions are no opening, continuity of traction components of stress, and no friction:

$$\omega(x) = 0 \quad (A24)$$
$$\tau^+(x) = \tau^-(x) \quad (A25)$$
$$\sigma^+(x) = \sigma^-(x) \quad (A26)$$
$$\tau(x)^{\pm} = 0. \quad (A27)$$

We further assume that in the absence of fault roughness, the fault experiences constant slip: $\delta(x) = \Delta$.

[46] The zeroth-order, or unperturbed solution, is thus

$$u_x^{(0)}(x, y) = 0.5\Delta\,\text{sgn}(y), \quad u_y^{(0)}(x, y) = 0, \quad (A28)$$
$$\sigma_{xx}^{(0)}(x, y) = \sigma_{xx}^0, \quad \sigma_{yy}^{(0)}(x, y) = \sigma_{yy}^0, \quad \sigma_{xy}^{(0)}(x, y) = 0. \quad (A29)$$

For this solution, equations (A18)–(A21) simplify to

$$\delta(x) = \Delta + [\hat{u}_x](x)$$
$$+ [\check{u}_x](x) + h(x)[\hat{u}_{x,y}](x) + m(x)[\hat{u}_y](x), \quad (A30)$$

$$\omega(x) = [\hat{u}_y](x) - m(x)\Delta$$
$$+ [\check{u}_y](x) + h(x)[\hat{u}_{y,y}](x) - m(x)[\hat{u}_x](x), \quad (A31)$$

$$\tau^{\pm}(x) = \hat{\sigma}_{xy}(x, 0^{\pm}) - m(x)\sigma_D$$
$$+ \check{\sigma}_{xy}(x, 0^{\pm}) + h(x)\hat{\sigma}_{xy,y}(x, 0^{\pm})$$
$$- m(x)[\hat{\sigma}_{xx}(x, 0^{\pm}) - \hat{\sigma}_{yy}(x, 0^{\pm})], \quad (A32)$$

$$\sigma^{\pm}(x) = -\sigma_{yy}^0 - \hat{\sigma}_{yy}(x, 0^{\pm})$$
$$- \check{\sigma}_{yy}(x, 0^{\pm}) - h(x)\hat{\sigma}_{yy,y}(x, 0^{\pm})$$
$$+ 2m(x)\hat{\sigma}_{xy}(x, 0^{\pm}) - m^2(x)\sigma_D. \quad (A33)$$

[47] Substituting equations (A30)–(A33) into the interface conditions (A24)–(A27), and dropping $O(\epsilon^2)$ terms, we obtain the following conditions for the first-order problem:

$$[\hat{u}_y](x) = m(x)\Delta, \quad (A34)$$
$$[\hat{\sigma}_{xy}](x) = 0, \quad (A35)$$
$$[\hat{\sigma}_{yy}](x) = 0, \quad (A36)$$
$$\hat{\sigma}_{xy}(x, 0) = m(x)\sigma_D. \quad (A37)$$

Note that because $\hat{\sigma}_{xy}$ is continuous across $y = 0$ (equation A35), there is no need to use $\pm$ in equation (A37) to distinguish between field values on the two sides of $y = 0$. We employ this notational simplification in the remainder of this Appendix.

[48] This problem is solved in the Fourier domain, and we define the transform of the fault profile and its slope as

$$H(k) = \int_{-\infty}^{\infty} h(x)e^{-ikx}\,dx, \quad (A38)$$

$$M(k) = \int_{-\infty}^{\infty} m(x)e^{-ikx}\,dx. \quad (A39)$$

Note that $M(k) = ikH(k)$.

[49] Fourier transforming the first-order interface conditions (A34)–(A37) yields

$$[\hat{U}_y](k) = M(k)\Delta, \tag{A40}$$

$$[\hat{\Sigma}_{xy}](k) = 0, \tag{A41}$$

$$[\hat{\Sigma}_{yy}](k) = 0, \tag{A42}$$

$$\hat{\Sigma}_{xy}(k,0) = M(k)\sigma_D. \tag{A43}$$

Combining these with the general elasticity solutions (A8)–(A12), we obtain the first-order solution in the transform domain. The displacement and stress along the interface are

$$\hat{U}_x^{\pm}(k,0) = \pm(1-\nu)\frac{\sigma_D}{G}\frac{|k|}{ik}H(k) - \frac{1-2\nu}{4(1-\nu)}\frac{|k|}{ik}M(k)\Delta, \tag{A44}$$

$$\hat{U}_y^{\pm}(k,0) = -\frac{1-2\nu}{2}\frac{\sigma_D}{G}H(k) \pm \frac{1}{2}M(k)\Delta, \tag{A45}$$

$$\hat{\Sigma}_{xx}^{\pm}(k,0) = \pm 2\sigma_D\frac{|k|}{ik}M(k) - \frac{G}{2(1-\nu)}|k|M(k)\Delta, \tag{A46}$$

$$\hat{\Sigma}_{yy}(k,0) = -\frac{G}{2(1-\nu)}|k|M(k)\Delta, \tag{A47}$$

$$\hat{\Sigma}_{xy}(k,0) = M(k)\sigma_D. \tag{A48}$$

Inverting the above transforms yields

$$\hat{u}_x^{\pm}(x,0) = \pm(1-\nu)\frac{\sigma_D}{G}\mathcal{H}[h(x)] - \frac{1-2\nu}{4(1-\nu)}\mathcal{H}[m(x)]\Delta, \tag{A49}$$

$$\hat{u}_y^{\pm}(x,0) = -\frac{1-2\nu}{2}\frac{\sigma_D}{G}h(x) \pm \frac{1}{2}m(x)\Delta, \tag{A50}$$

$$\hat{\sigma}_{xx}^{\pm}(x,0) = \pm 2\sigma_D\mathcal{H}[m(x)] - \frac{G}{2(1-\nu)}\mathcal{H}[m'(x)]\Delta, \tag{A51}$$

$$\hat{\sigma}_{yy}(x,0) = -\frac{G}{2(1-\nu)}\mathcal{H}[m'(x)]\Delta, \tag{A52}$$

$$\hat{\sigma}_{xy}(x,0) = m(x)\sigma_D, \tag{A53}$$

where the Hilbert transform of a function $g(x)$ is

$$\mathcal{H}[g(x)] = \frac{1}{\pi}\int_{-\infty}^{\infty}\frac{g(\xi)}{x-\xi}d\xi. \tag{A54}$$

[50] It is possible, at this point, to solve the complete second-order problem. However, we are only interested in calculating the roughness drag, and as we demonstrate in the next section, that task (for frictionless faults) requires only an expression for $\check{\sigma}_{xy}^{\pm}(x,0)$. That is obtained by substituting equation (A32) into the frictionless sliding condition (A27):

$$\check{\sigma}_{xy}^{\pm}(x,0) = -h(x)\hat{\sigma}_{xy,y}^{\pm}(x,0) + m(x)[\hat{\sigma}_{xx}^{\pm}(x,0) - \hat{\sigma}_{yy}(x,0)]. \tag{A55}$$

A4. Roughness Drag

[51] We are now poised to calculate the roughness drag, which is defined in the following way. The traction vector giving the force per unit area exerted by the top wall of the fault on the bottom wall is $\sigma_{ij}(x,h(x)^-)n_j(x)$, where $(n_x(x), n_y(x)) \approx (-m(x), 1 - m^2(x)/2)$ is the unit outward normal to the lower half-space, given to second-order accuracy. The net force (per unit distance in the z-direction) acting on the fault segment $-L/2 < x < L/2$ and opposing motion in the x direction is

$$F = \int_{-L/2}^{L/2} T(x)dx, \tag{A56}$$

$$T(x) = \sigma_{xj}(x,h(x)^-)n_j(x)\sqrt{1+m^2(x)}, \tag{A57}$$

where $\sqrt{1+m^2(x)}dx$ is the differential arc length. Dividing F by L gives the average shear stress resisting slip, and taking $L \to \infty$ gives the expectation value, $E[T(x)]$. For frictionless sliding, we define this as the roughness drag, τ^{drag}. For the more general case of sliding at constant friction coefficient f, the appropriate definition of roughness drag would be

$$\tau^{\mathrm{drag}} = E[T(x) - \sigma_{xy}^0], \tag{A58}$$

where $\sigma_{xy}^0 = f(-\sigma_{yy}^0)$ is the frictional resistance.

[52] To evaluate τ^{drag}, we expand $T(x)$ in (A57) to second-order accuracy:

$$\begin{aligned}T(x) = &\sigma_{xy}^0 + \hat{\sigma}_{xy}(x,0^-) - m(x)\sigma_{xx}^0 \\ &+ \check{\sigma}_{xy}(x,0^-) + h(x)\hat{\sigma}_{xy,y}(x,0^-) \\ &- m(x)\hat{\sigma}_{xx}(x,0^-).\end{aligned} \tag{A59}$$

Next, we set $\sigma_{xy}^0 = 0$, substitute $\check{\sigma}_{xy}(x,0^-)$ from (A55), and recognize that $E[m(x)] = 0$. The result is remarkably simple:

$$\tau^{\mathrm{drag}} = -E[m(x)\hat{\sigma}_{yy}(x,0)]. \tag{A60}$$

Using (A52) gives

$$\tau^{\mathrm{drag}} = \frac{G\Delta}{2(1-\nu)}E[m(x)\mathcal{H}[m'(x)]]. \tag{A61}$$

The expectation value can be rewritten [e.g., *Newland*, 1993] in terms of the power spectral density $P_m(k)$ of $m(x)$ as

$$\tau^{\mathrm{drag}} = \frac{G\Delta}{2\pi(1-\nu)}\int_0^{\infty} kP_m(k)dk. \tag{A62}$$

For self-similar faults, $P_m(k) = (2\pi)^3\alpha^2|k|^{-1}$ and the above integral diverges unless the upper limit of the wavenumber integral is bounded. That is equivalent to introducing a minimum roughness wavelength, $\lambda_{\min}$, which yields the desired expression for roughness drag:

$$\tau^{\mathrm{drag}} = 8\pi^3\alpha^2\frac{G}{1-\nu}\frac{\Delta}{\lambda_{\min}}. \tag{A63}$$

References

Anderson, E. M. (1951), *The Dynamics of Faulting*, 2nd ed., 206 pp., Oliver and Boyd, Edinburgh, Scotland.

Beeler, N. M., and T. E. Tullis (1996), Self-healing pulse in dynamic rupture models due to velocity-dependent strength, *Bull. Seism. Soc. Am.*, 86(4), 1130–1148.

Beeler, N. M., T. E. Tullis, and D. L. Goldsby (2008), Constitutive relationships and physical basis of fault strength due to flash heating, *J. Geophys. Res.*, 113, B01401, doi:10.1029/2007JB004988.

Bistacchi, A., W. A. Griffith, S. A. F. Smith, G. Di Toro, R. Jones, and S. Nielsen (2011), Fault roughness at seismogenic depths from LIDAR and photogrammetric analysis, *Pure Appl. Geophys.*, 168, 2345–2363, doi:10.1007/s00024-011-0301-7.

Brodsky, E. E., J. J. Gilchrist, A. Sagy, and C. Collettini (2011), Faults smooth gradually as a function of slip, *Earth Planet. Sc. Lett.*, 302, 185–193, doi:10.1016/j.epsl.2010.12.010.

Brown, S. R., and C. H. Scholz (1985), Broad bandwidth study of the topography of natural rock surfaces, *J. Geophys. Res.*, 90(B14), 12,575–12,582, doi:10.1029/JB090iB14p12575.

Byerlee, J. (1978), Friction of rocks, *Pure Appl. Geophys.*, 116, 615–626.

Byerlee, J. (1990), Friction, overpressure and fault normal compression, *Geophys. Res. Lett.*, *17*(12), 2109–2112, doi:10.1029/GL017i012p02109.

Candela, T., F. Renard, M. Bouchon, A. Brouste, D. Marsan, J. Schmittbuhl, and C. Voisin (2009), Characterization of fault roughness at various scales: Implications of three-dimensional high resolution topography measurements, *Pure Appl. Geophys.*, *166*, 1817–1851, doi:10.1007/s00024-009-0521-2.

Candela, T., F. Renard, M. Bouchon, J. Schmittbuhl, and E. E. Brodsky (2011), Stress drop during earthquakes: Effect of fault roughness scaling, *Bull. Seism. Soc. Am.*, *101*, 2369–2387, doi:10.1785/0120100298.

Candela, T., F. Renard, Y. Klinger, K. Mair, J. Schmittbuhl, and E. E. Brodsky (2012), Roughness of fault surfaces over nine decades of length scales, *J. Geophys. Res.*, *117*, B08409, doi:10.1029/2011JB009041.

Carpenter, B. M., C. Marone, and D. M. Saffer (2011), Weakness of the San Andreas Fault revealed by samples from the active fault zone, *Nat. Geosci.*, *4*, 251–254, doi:10.1038/ngeo1089.

Chester, F. M., and J. S. Chester (2000), Stress and deformation along wavy frictional faults, *J. Geophys. Res.*, *105*(B10), 23,421–23,430, doi:10.1029/2000JB900241.

Cochard, A., and R. Madariaga (1996), Complexity of seismicity due to highly rate-dependent friction, *J. Geophys. Res.*, *101*(B11), 25,321–25,336, doi:10.1029/96JB02095.

Collettini, C., and R. H. Sibson (2001), Normal faults, normal friction? *Geology*, *29*(10), 927–930, doi:10.1130/0091-7613(2001)029<0927:NFNF>2.0.CO;2.

Collettini, C., A. Niemeijer, C. Viti, and C. Marone (2009), Fault zone fabric and fault weakness, *Nature*, *462*, 907–910, doi:10.1038/nature08585.

Di Toro, G., D. L. Goldsby, and T. E. Tullis (2004), Friction falls toward zero in quartz rock as slip velocity approaches seismic rates, *Nature*, *427*, 436–439, doi:10.1038/nature02249.

Di Toro, G., R. Han, N. De Paola, S. Nielsen, K. Mizoguchi, F. Ferri, M. Cocco, and T. Shimamoto (2011), Fault lubrication during earthquakes, *Nature*, *471*, 494–498, doi:10.1038/nature09838.

Dieterich, J. H. (1992), Earthquake nucleation on faults with rate- and state-dependent strength, *Tectonophysics*, *211*, 115–134, doi:10.1016/0040-1951(92)90055-B.

Dieterich, J. H., and D. E. Smith (2009), Nonplanar faults: Mechanics of slip and off-fault damage, *Pure Appl. Geophys.*, *166*, 1799–1815, doi:10.1007/s00024-009-0517-y.

Dunham, E. M., D. Belander, C. Lin, and J. E. Kozdon (2011a), Earthquake ruptures with strongly rate-weakening friction and off-fault plasticity, part 1: Planar faults, *Bull. Seism. Soc. Am.*, *101*, 2296–2307, doi:10.1785/0120100075.

Dunham, E. M., D. Belander, C. Lin, and J. E. Kozdon (2011b), Earthquake ruptures with strongly rate-weakening friction and off-fault plasticity, part 2: Rough faults, *Bull. Seism. Soc. Am.*, *101*, 2308–2322, doi:10.1785/0120100076.

Fang, Z., J. H. Dieterich, and G. Xu (2010), Effect of initial conditions and loading path on earthquake nucleation, *J. Geophys. Res.*, *115*, B06313, doi:10.1029/2009JB006558.

Faulkner, D. R., and E. H. Rutter (2001), Can the maintenance of overpressured fluids in large strike-slip fault zones explain their apparent weakness? *Geology*, *29*, 503–506, doi:10.1130/0091-7613(2001)029<0503:CTMOOF>2.0.CO;2.

Gabriel, A. A., J. P. Ampuero, L. A. Dalguer, and P. M. Mai (2012), The transition of dynamic rupture styles in elastic media under velocity-weakening friction, *J. Geophys. Res.*, *117*, B09311, doi:10.1029/2012JB009468.

Gabriel, A. A., J. P. Ampuero, L. A. Dalguer, and P. M. Mai (2013), Source properties of dynamic rupture pulses with off-fault plasticity, *J. Geophys. Res. Solid Earth*, doi:10.1002/jgrb.50213.

Goldsby, D. L., and T. E. Tullis (2011), Flash heating leads to low frictional strength of crustal rocks at earthquake slip rates, *Science*, *334*, 216–218, doi:10.1126/Science.1207902.

Gusman, A. R., M. Fukuoka, Y. Tanioka, and S. Sakai (2013), Effect of the largest foreshock (m_w 7.3) on triggering the 2011 Tohoku earthquake (m_w 9.0), *Geophys. Res. Lett.*, *40*, 497–500, doi:10.1002/grl.50153.

Hennings, P., A. Patricia, P. Paul, Z. Chris, R. J. Ray, A. Hugh, K. Roland, L. Bob, and H. Elliott (2012), Relationship between fractures, fault zones, stress, and reservoir productivity in the Suban gas field, Sumatra, Indonesia, *AAPG Bull.*, *96*(4), 753–772, doi:10.1306/08161109084.

Hickman, S., and M. Zoback (2004), Stress orientations and magnitudes in the SAFOD pilot hole, *Geophys. Res. Lett.*, *31*, L15S12, doi:0.1029/2004GL020043.

Hirose, T., and T. Shimamoto (2005), Growth of a molten zone as a mechanism of slip weakening of simulated faults in gabbro during frictional melting, *J. Geophys. Res.*, *110*, B05202, doi:10.1029/2004JB003207.

Jaeger, J., N. Cook, and R. Zimmerman (2007), *Fundamentals of Rock Mechanics*, 4th ed., 488 p., Blackwell Publishing Ltd, Malden, Mass.

Kozdon, J. E., E. M. Dunham, and J. Nordström (2011), Interaction of waves with frictional interfaces using summation-by-parts difference operators: Weak enforcement of nonlinear boundary conditions, *J. Sci. Comput.*, *50*, 341–367, doi:10.1007/s10915-011-9485-3.

Kozdon, J. E., E. M. Dunham, and J. Nordström (2012), Simulation of dynamic earthquake ruptures in complex geometries using high-order finite difference methods, *J. Sci. Comput.*, *55*, 92–124, doi:10.1007/s10915-012-9624-5.

Lapusta, N., and J. R. Rice (2003), Nucleation and early seismic propagation of small and large events in a crustal earthquake model, *J. Geophys. Res.*, *108*(B4), 2205, doi:10.1029/2001JB000793.

Lee, J.-J., and R. L. Bruhn (1996), Structural anisotropy of normal fault surfaces, *J. Struct. Geol.*, *18*(8), 1043–1059, doi:10.1016/0191-8141(96)00022-3.

Lykotrafitis, G., A. J. Rosakis, and G. Ravichandran (2006), Self-healing pulse-like shear ruptures in the laboratory, *Science*, *313*, 1765–1768, doi:10.1126/science.1128359.

Morrow, C. A., D. E. Moore, and D. A. Lockner (2000), The effect of mineral bond strength and adsorbed water on fault gouge frictional strength, *Geophys. Res. Lett.*, *27*, 815–818, doi:10.1029/1999GL008401.

Murray, J., and P. Segall (2002), Testing time-predictable earthquake recurrence by direct measurement of strain accumulation and release, *Nature*, *419*, 287–291, doi:10.1038/nature00984.

Newland, D. E. (1993), *An Introduction to Random Vibrations, Spectral and Wavelet Analysis*, 3rd ed., 477 pp., Longman Scientic and Technical, Essex, U.K.

Noda, H., E. M. Dunham, and J. R. Rice (2009), Earthquake ruptures with thermal weakening and the operation of major faults at low overall stress levels, *J. Geophys. Res.*, *114*, B07302, doi:10.1029/2008JB006143.

Nye, J. F. (1969), A calculation on the sliding of ice over a wavy surface using a Newtonian viscous approximation, *Proc. Roy. Soc. London A*, *311*(1506), 445–467, doi:10.1098/rspa.1969.0127.

Nye, J. F. (1970), Glacier sliding without cavitation in a linear viscous approximation, *Proc. Roy. Soc. London A*, *315*(1522), 381–403, doi:10.1098/rspa.1970.0050.

Poliakov, A. N. B., R. Dmowska, and J. R. Rice (2002), Dynamic shear rupture interactions with fault bends and off-axis secondary faulting, *J. Geophys. Res.*, *107*(B11), 2295, doi:10.1029/2001JB000572.

Power, W. L., and T. E. Tullis (1988), Roughness and wear during brittle faulting, *J. Geophys. Res.*, *93*(B11), 15,268–15,278, doi:10.1029/JB093iB12p15268.

Power, W. L., and T. E. Tullis (1991), Euclidean and fractal models for the description of rock surface roughness, *J. Geophys. Res.*, *96*(B1), 415–424, doi:10.1029/90JB02107.

Power, W. L., and T. E. Tullis (1995), Review of the fractal character of natural fault surfaces with implications for friction and the evolution of fault zones, in *Fractals in the Earth Sciences*, edited by C. C. Barton and P. R. L. Pointe, chap. 5, pp. 89–105, Plenum Press, New York.

Renard, F., C. Voisin, D. Marsan, and J. Schmittbuhl (2006), High resolution 3D laser scanner measurements of a strike-slip fault quantify its morphological anisotropy at all scales, *Geophys. Res. Lett.*, *33*, L04305, doi:10.1029/2005GL025038.

Rice, J. R. (1992), Fault stress states, pore pressure distributions, and the weakness of the San Andreas Fault, in *Fault Mechanics and Transport Properties of Rocks*, edited by B. Evans and T.-F. Wong, chap. 20, pp. 475–503, Academic Press, San Diego.

Rice, J. R. (1993), Spatio-temporal complexity of slip on a fault, *J. Geophys. Res.*, *98*(B6), 9885–9907, doi:10.1029/93JB00191.

Rice, J. R. (2006), Heating and weakening of faults during earthquake slip, *J. Geophys. Res.*, *111*, B05311, doi:10.1029/2005JB004006.

Rice, J. R., C. G. Sammis, and R. Parsons (2005), Off-fault secondary failure induced by a dynamic slip-pulse, *Bull. Seism. Soc. Am.*, *95*, 109–134, doi:10.1785/0120030166.

Rubin, A. M., and J. P. Ampuero (2005), Earthquake nucleation on (aging) rate and state faults, *J. Geophys. Res.*, *110*, B11312, doi:10.1029/2005JB003686.

Sagy, A., and E. E. Brodsky (2009), Geometric and rheological asperities in an exposed fault zone, *J. Geophys. Res.*, *114*, B02301, doi:10.1029/2008JB005701.

Sagy, A., E. E. Brodsky, and G. J. Axen (2007), Evolution of fault-surface roughness with slip, *Geology*, *35*, 283–286, doi:10.1130/G23235A.1.

Saucier, F., E. Humphreys, and R. Weldon (1992), Stress near geometrically complex strike-slip faults: Application to the San Andreas Fault at Cajon Pass, southern California, *J. Geophys. Res.*, *97*(B4), 5081–5094, doi:10.1029/91JB02644.

Shi, Z., and S. Day (2013), Three-dimensional simulations of dynamic rupture on rough faults, *J. Geophys. Res. Solid Earth*, *118*, 1122–1141, doi:10.1002/jgrb.50094.

Shimazaki, K., and T. Nakata (1980), Time-predictable recurrence model for large earthquakes, *Geophys. Res. Lett.*, *7*(4), 279–282, doi:10.1029/GL007i004p00279.

Sibson, R. H. (1985), A note on fault reactivation, *J. Struct. Geol.*, *7*(6), 751–754, doi:10.1016/0191-8141(85)90150-6.

Sibson, R. H. (1994), An assessment of field evidence for 'Byerlee' friction, *Pure Appl. Geophys.*, *142*, 645–662, doi:10.1007/BF00876058.

Sibson, R. H., and G. Xie (1998), Dip range for intracontinental reverse fault ruptures: Truth not stranger than friction? *Bull. Seism. Soc. Am.*, *88*(4), 1014–1022.

Townend, J., and M. D. Zoback (2000), How faulting keeps the crust strong, *Geology*, *28*, 399–402, doi:10.1130/0091-7613(2000)28<399:HFKTCS>2.0.CO;2.

Townend, J., and M. D. Zoback (2004), Regional tectonic stress near the San Andreas Fault in central and Southern California, *Geophys. Res. Lett.*, *31*, L15S11, doi:10.1029/2003GL018918.

Tsutsumi, A., and T. Shimamotom (1997), High velocity frictional properties of gabbro, *Geophys. Res. Lett.*, *24*, 699–702, doi:10.1029/97GL00503.

Zheng, G., and J. R. Rice (1998), Conditions under which velocity-weakening friction allows a self-healing versus a cracklike mode of rupture, *Bull. Seism. Soc. Am.*, *88*(6), 1466–1483.

Zoback, M. D., S. H. Hickman, and W. L. Ellsworth (2010), Scientific drilling into the San Andreas Fault zone, *Eos Trans. AGU*, *91*, 197–199, doi:10.1029/2010EO220001.